



SUBJECT AREAS:  
BIOTECHNOLOGY  
BIOCHEMISTRY  
BIOPHYSICS  
MEDICAL RESEARCH

Received  
8 August 2012

Accepted  
11 December 2012

Published  
21 January 2013

Correspondence and  
requests for materials  
should be addressed to  
G.R. (gren@lbl.gov)

# Peptide-Conjugation Induced Conformational Changes in Human IgG1 Observed by Optimized Negative-Staining and Individual-Particle Electron Tomography

Huimin Tong<sup>1,2</sup>, Lei Zhang<sup>2</sup>, Allan Kaspar<sup>3</sup>, Matthew J. Rames<sup>2</sup>, Liqing Huang<sup>1</sup>, Gary Woodnutt<sup>3</sup> & Gang Ren<sup>2</sup>

<sup>1</sup>MOE Key Laboratory for Non-equilibrium Synthesis and Modulation of Condensed Matter, School of Science, Xi'an Jiaotong University, Xi'an 710049, China, <sup>2</sup>The Molecular Foundry, Lawrence Berkeley National Laboratory, Berkeley CA 94720, <sup>3</sup>Pfizer Inc, CovX Research LLC, San Diego, CA 92121.

Peptides show much promise as potent and selective drug candidates. Fusing peptides to a scaffold monoclonal antibody produces a conjugated antibody which has the advantages of peptide activity yet also has the pharmacokinetics determined by the scaffold antibody. However, the conjugated antibody often has poor binding affinity to antigens that may be related to unknown structural changes. The study of the conformational change is difficult by conventional techniques because structural fluctuation under equilibrium results in multiple structures co-existing. Here, we employed our two recently developed electron microscopy (EM) techniques: optimized negative-staining (OpNS) EM and individual-particle electron tomography (IPET). Two-dimensional (2D) image analyses and three-dimensional (3D) maps have shown that the domains of antibodies present an elongated peptide-conjugated conformational change, suggesting that our EM techniques may be novel tools to monitor the structural conformation changes in heterogeneous and dynamic macromolecules, such as drug delivery vehicles after pharmacological synthesis and development.

Peptides have become central in developing new drug delivery due to their high specificity and low toxicity profile<sup>1</sup>. Traditionally only a small portion of oral medication reaches the target organ. Because of this there is a need to enhance the selective uptake of peptides/drugs by target: tissues, cells, or macromolecules (such as antibodies, peptides, and liposomes) which are usually used as synthetic targeted delivery devices<sup>2,3</sup>. Targeted drug delivery has been recognized as a novel approach in treating or controlling some chronic diseases<sup>4,5</sup> thereby reducing side effects in the body via concentrating the medication in the tissues of interest. Developing synthetic vehicles can be a challenging, costly, and time-intensive process because binding the peptide/drug to the carrier, such as a scaffold IgG1 antibody (monoclonal antibody h38C2), often causes unwanted conformational changes<sup>6</sup>. For instance, Pfizer CovX Research LLC developed a peptide conjugated antibody that had shown promise as a potent and selective drug candidate for treating tumors<sup>7,8</sup>. However, the peptide-conjugated antibodies did not show effector function (e. g. antibody-dependent cellular cytotoxicity, ADCC) against cell surface targets, nor did the pharmacokinetics of the conjugated peptide match the pharmacokinetics of the antibody scaffold, leading to the suspicion that the conjugation with the peptide may have introduced structural changes in the antibody.

Monitoring the structure of synthetic vehicles may improve the efficiency of the manufacturing process, reduce cost, and avoid dead-end development paths. Current techniques in structural determination (such as X-ray crystallography, nuclear magnetic resonance (NMR) and small-angle scattering) have limited power, capability, or efficiency in obtaining the structures of synthetic drug delivery vehicles, such as antibodies or lipoproteins that are structurally dynamic and heterogeneous. For example, the antibody native state is not defined by a single rigid conformation but instead with an ensemble of similar conformations that co-exist at equilibrium<sup>9,10</sup>. Electron microscopy (EM) is a powerful tool that allows direct visualization of each individual particle. Cryo-electron



microscopy (cryo-EM) can provide the images of proteins embedded in vitrified buffer environments<sup>11</sup>; however, the contrast of these images is low. A class-averaging computational method is commonly used to increase the contrast by averaging hundreds to thousands of images of macromolecular particles<sup>12,13</sup>. However, the class-average method is limited by the following facts: i) macromolecules in solution are naturally dynamic and fluctuate; ii) 2D images of macromolecules are mathematically insufficient to determine their 3D orientations (as an extreme case, a right-handed 3D object has many shared 2D projections with a left-hand object); and iii) the total number of classes (or sampling angle) in a class-average strategy is defined based on personal experience and judgment. In theory, a limited number of sampling angles is insufficient or inaccurate to classify a completely random distributed object, especially when object has its own structural dynamics.

A fundamental solution in the structural determination of dynamic macromolecules should rely on the determination of each individual particle's structure instead of averaging tens of thousands of different particles. Two recently reported sample preparation protocols, i.e. the optimized negative-staining protocol (OpNS)<sup>14,15</sup> and the cryo-positive-staining (cryo-PS) protocol<sup>16</sup>, can be used for high-throughput and high-resolution imaging of individual small proteins. OpNS protocol is refined from the conventional NS protocol and provides similar (<~5% difference) particle images in size and shape with that from cryo-EM<sup>14,15</sup>, which was demonstrated with lipoproteins. This OpNS protocol has also been used to study the dynamics of antibodies<sup>17</sup> and has revealed the mechanism of a small protein, 53kDa cholesteryl ester transfer protein (CETP)<sup>16</sup>. The cryo-PS-EM has been developed by combining the OpNS and conventional cryo-EM protocols for directly visualization of the secondary structure of small proteins<sup>16</sup>. A recently reported high-resolution computational reconstruction method, individual-particle electron tomography (IPET) allows one to achieve a high-resolution 3D density map of a single-instance particle from a series of tilted viewing images of this particle by electron tomography<sup>17</sup>. IPET can achieve: i) a sub-nanometer resolution 3D map of an individual protein from a set of computer-simulated cryo-electron tomography (cryo-ET) images with a signal-to-noise ratio (SNR) under 0.2; ii) highest resolution (~14 Å) 3D map of an individual antibody from a set of OpNS images; and iii) ~36 Å resolution 3D map of an individual small particle, nascent high-density lipoprotein (HDL, molecular mass ~140–220 kDa) from a set of real experimental cryo-ET images<sup>17</sup>. IPET is a novel and robust strategy that does not require a pre-given initial model, class averaging of multiple molecules, or an extended ordered lattice, but can tolerate small tilt-errors for high-resolution structure determination of an individual “snapshot” molecule. By comparing the “snap-shot” structures from different particles, IPET opens the door to experimentally study the protein fluctuation and dynamics in solution. Here, we employed the OpNS protocol and IPET method to study the structure of small and dynamic peptide-conjugated antibodies.

## Results

**High-resolution images of unconjugated IgG antibodies by optimized-negative-staining electron microscopy (OpNS-EM).** Unconjugated antibody, monoclonal antibody IgG subclass 1, h38C2 (humanized version of m38C2) was prepared by OpNS, and examined by EM. After Gaussian low-pass filtering, the survey OpNS-EM image (Fig. 1A) and selected particles (Fig. 1B) of unconjugated antibody (scaffold) samples show a “Y” shaped antibody component with three globular domains, corresponding to two  $F_{ab}$  domains linked to one  $F_c$  domain. The size of the antibody particles is ~150–200 Å, in which each domain size is ~50–80 Å. Interestingly, more than a half of raw particle images show significant structural details, including particle orientation and lower density holes (Fig. 1). At specific viewing orientations,

manual masks were applied on the raw particle images (Fig. 1C) near the particle boundary to reduce outside noise (Fig. 1D), revealing that the particle outer features are remarkably similar to crystal structure of an IgG2a antibody (PDB entry 1IGT)<sup>18</sup>, an anti-canine lymphoma monoclonal antibody (mab231) (Fig. 1E). For example, the particle domain features including the low-density holes, are similar to the domains and holes formed by  $\beta$ -sheet strands in the crystal structure (Fig. 1E).

**High-resolution images of peptide-conjugated IgG antibodies by OpNS-EM.** Conjugated antibody (peptide-conjugated monoclonal IgG1 antibody h38C2) samples were prepared and examined by OpNS-EM, the survey image after Gaussian low-pass filter (Fig. 2A) and selected particles (Fig. 2B) show a “Y” shape with a size of ~160–220 Å, similar to those of the unconjugated antibodies. However, each domain in these “Y”-shaped particles have a diameter ~40–90 Å that seems longer and thinner than the domain of unconjugated antibodies (50–80 Å). By zooming in on the raw particle images, only some domains show a hole (Fig. 2B), and two domains seem closer to each other, yet farther from the third one. To generate a conclusive picture, we analyzed the differences between the unconjugated and conjugated antibodies from the following four aspects: i) statistical domain size; ii) domain shape; iii) the angles between  $F_{ab}$  and  $F_c$  domains; iv) 3D density maps.

**Domain size remains unchanged after peptide conjugation.** To quantitatively analyze the conformational changes in domain size and shape of particles, all isolated unconjugated and conjugated antibody particles were selected and windowed from charge-coupled device (CCD) frames with no apparent astigmatism or drift. The size of domains in each particle were determined by measuring diameters along two perpendicular directions, one being the longest dimension (Fig. 3A) as previously used<sup>14,15</sup>. The morphology of domains in the particles was statistically analyzed by size and shape.

Size analysis is calculated with the geometric average of the longest diameter and its perpendicular diameter, to represent particle size (Fig. 3A). Since the geometric average is the square root of the product of two diameters, it reflects the in-plane area of a particle on the supporting film. This 2D dimensional measurement (in-plane area) should more accurately reflect the 3D particle volume than any one-dimensional measurement.

The distribution of geometric averages of unconjugated antibodies (a total of ~250 particles) showed that more than 90% of domains were between ~50 Å and ~80 Å, with the peak population (~11.6% of particles) occurring at  $66.8 \pm 1.0$  Å (the error  $\pm 1.0$  Å is due to the sample step of 2.0 Å) (Fig. 3B). In contrast, the distribution of geometric averages of conjugated antibodies (a total of ~332 particles) showed that more than 90% of domains were between ~48 Å and ~78 Å, with the peak population (~10.8% of particles) occurring at  $64.2 \pm 1.0$  Å (Fig. 3B). The histogram of geometric means shows the size of the domains between unconjugated and conjugated antibodies remains similar (~3.9% difference).

**Domain shape changes after peptide conjugation.** Domain shape analysis calculates the ratio between the longest diameter and the perpendicular diameter of each domain as described<sup>14,15</sup>. The distribution of diameter ratios of unconjugated antibodies shows that more than 90% of the imaged domains have a ratio of ~1.0–1.8, and the peak population (~21.6%) at ratio of  $1.28 \pm 0.05$  (the error  $\pm 0.05$  is due to the sample step of 0.10) (Fig. 3C) suggesting an ellipsoidal shape for the domains of unconjugated antibodies (Fig. 1).

In contrast, the distribution of diameter ratios of conjugated antibodies shows that more than 90% of domain images have a ratio in range of ~1.0–2.2, and the peak population (~12.5%) at a ratio of  $1.53 \pm 0.05$  (Fig. 3C), also suggesting an ellipsoidal shape of domains for the conjugated particles (Fig. 2). However, the

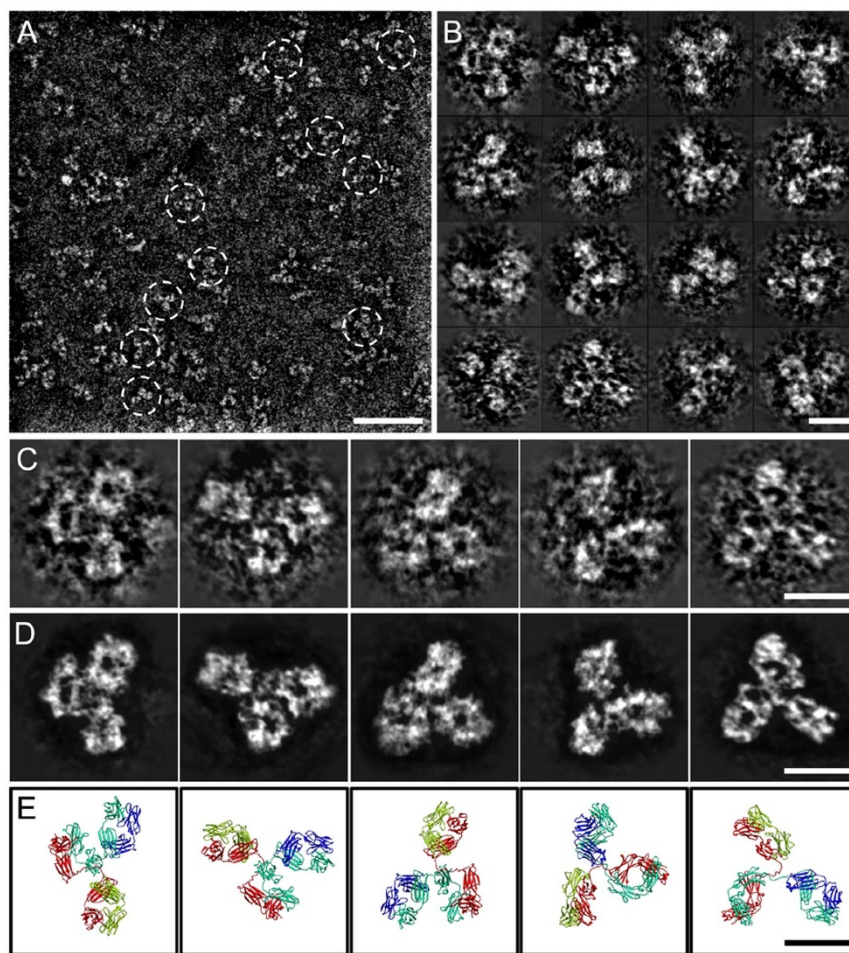


**Figure 1 | High-resolution images of unconjugated antibodies by OpNS-EM.** (A) Survey view of the unconjugated antibody (dashed circles). Particles are “Y”-shaped containing three globular circular or oval domains. (B) 16 representative views of selected and windowed individual raw particles of unconjugated antibody. (C) Five high-resolution and raw particle images of selected and windowed individual unconjugated antibody particles and (D) their corresponding noise-reduced images via a manual noise-reduction around the particle images edges for easier-visualization. (E) These latter images were compared with the crystal structure of IgG antibody (PDB entry 1IGT) at similar orientations. The EM images present many similar features with the crystal structure, i.e., the domain spacing distribution and circular holes. Scale bars: A, 50 nm; B–E, 10 nm.

histogram with polynomial regression curves shows a significant difference in domain shape between conjugated antibodies and unconjugated antibodies. Statistical analysis indicates that the domain shape of the conjugated antibodies was elongated  $\sim 20\%$  after peptide conjugation. Considering the peak sizes of domains are around 64 – 67 Å, the 20% elongation corresponds to an  $\sim 13$  Å conformational change after peptide conjugation.

**Domain fluctuation restricted after peptide conjugation.** To quantitatively analyze the spacing freedom fluctuations of antibody domains, we measured the angle that two  $F_{ab}$  domains make against the  $F_c$  domain. Measurements were performed by defining the centers of three domains of each particle, then computing the angles between the  $F_{ab}^1-F_c-F_{ab}^2$  domains based on their center coordinates (Fig. 3D). The angle distribution histogram of unconjugated antibodies shows that more than 90% of the imaged domains have an angle  $\sim 39^\circ-99^\circ$ , with the peak population ( $\sim 11.6\%$ ) at an angle of  $\sim 57.8 \pm 2.5^\circ$  (the error  $\pm 2.5^\circ$  is due to the sample step of  $5.0^\circ$ ) (Fig. 3E). The histogram for conjugated antibodies shows that more than 90% of the imaged domains have an angle in the range of  $\sim 29^\circ-94^\circ$ , with the peak population ( $\sim 10.5\%$ ) at an angle of  $\sim 45.2 \pm 2.5^\circ$  (Fig. 3E). The distribution supported an observed difference, in which the conjugated antibodies showed a peak of  $45.2^\circ$ , which is smaller than the unconjugated antibodies peak of  $\sim 57.8^\circ$ . The

smaller angle in conjugated antibodies indicates that the spacing freedom of antibodies may be restricted by the peptide binding.

The above statistical analyses, which are based on 2D images of antibodies, suggest that each antibody domain changed its conformation after the peptide conjugation, restricting its fluctuation.

### 3D reconstruction of an individual unconjugated IgG antibody by individual-particle electron tomography (IPET).

In order to study the conformational changes (from a 3D view instead of 2D projections described above) of the antibody domains introduced by peptide conjugation, the unconjugated OpNS sample was imaged from a series of tilted-angles. By tracking a targeted individual unconjugated antibody, we reconstructed its 3D density map from tilted image views via IPET (Fig. 4A). IPET is a novel technique to determine the 3D image of an individual macromolecule<sup>17</sup>. Since the 3D density map is from a single flash-fixed particle kept in the same conformation during ET imaging, the 3D map shows the structure of this targeted particle which is dynamically, conformationally, and heterogeneously locked<sup>17</sup>. Although the 3D density map of this antibody has been previously published to describe the IPET methodology<sup>17</sup>, this is the highest resolution map achieved from one single small macromolecular particle that has ever been obtained by ET before, impacting the EM and ET fields. Some scientists were interested in even more detailed procedures, such as raw and

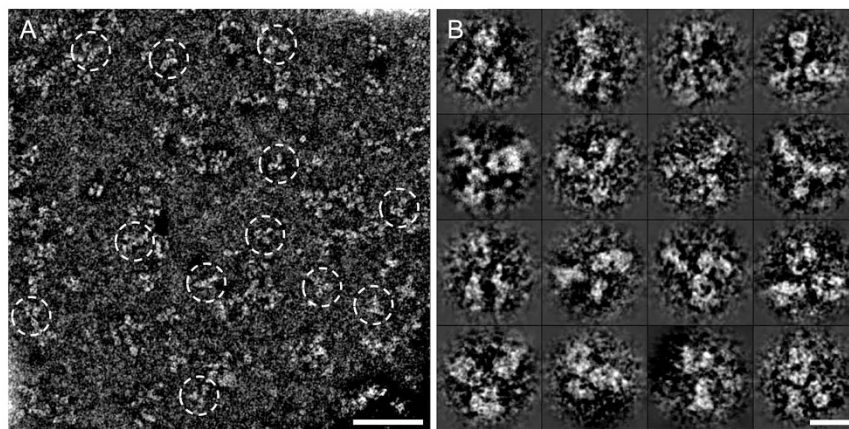


**Figure 2 | High-resolution images of peptide-conjugated antibodies by OpNS-EM.** (A) Survey view of the peptide-conjugated antibody (dashed circles). Particles are again “Y”-shaped containing three globular circular or oval domains. (B) 16 representative views of selected and windowed raw particles of peptide-conjugated antibody. Scale bars: A, 50 nm; B, 10 nm.

aligned 2D images, intermediate 3D maps and structural interpolation. Considering this, we compressed the step-by-step images and maps into a detailed movie (**Supplementary Video S1**).

Intra-Fourier shell correlation (intra-FSC) analysis<sup>17</sup> showed that the resolution of the 3D map was  $\sim 14.1$  Å (**Supplementary Fig. S1**). The 3D map of an individual antibody with density contour level close to the antibody molecular weight shows that the particle has three domains. The diameters of these domains are:  $\sim 61$ – $72$  Å (geometric average  $\sim 67$  Å, diameter ratio  $\sim 1.18$ ),  $\sim 70$ – $76$  Å (geometric average  $\sim 73$  Å, diameter ratio  $\sim 1.10$ ) and  $\sim 67$ – $85$  Å (geometric average  $\sim 75$  Å, diameter ratio  $\sim 1.27$ ) (**Fig. 4B**). A lower density hole in each of the three domains has diameter of  $\sim 20$ – $35$  Å (**Fig. 4B**). Two holes are similar in size (geometric average  $\sim 23$  Å), but obviously smaller than the third hole (geometric average  $\sim 32$  Å) (**Fig. 4B**). These structural features are consistent to the crystal structure of the IgG antibody (PDB entry 1IGT)<sup>19</sup>, in which the holes of two  $F_{ab}$  domains are much smaller than that of the  $F_c$  domain. Although the 3D map is similar to the crystal structure of the IgG antibody as shown in the 2D images (**Fig. 1C–E**), the domain location and orientation do not show a perfect match. This is because the antibody native state is not defined by a single rigid conformation of crystal structure, but instead with an ensemble of similar conformations that co-exist at equilibrium. To obtain a new structure of this antibody, we separated each domain from the crystal structure, inserted them into their corresponding domain density maps based on a rigid-body fit by Chimera<sup>20</sup>, and then manually repaired the connecting loop structures among the domains to achieve the new conformational structure. The near perfect match between the crystal domain structures and domain 3D density maps (**Fig. 4C**, **Supplementary Video S1**) suggests a new conformation of the antibody in solution was discovered.

Using IPET, we reconstructed another 3D density map from another targeted individual unconjugated antibody (**Fig. 4D**)<sup>17</sup>. This  $\sim 14.6$  Å resolution 3D map corresponds to the molecular weight contour density level (**Fig. 4E**), and shows a similar structure to that of the first targeted antibody particle in shape and size. The diameter of the domains are:  $\sim 50$ – $70$  Å (geometric average  $\sim 59$  Å, diameter ratio  $\sim 1.39$ ),  $\sim 59$ – $63$  Å (geometric average  $\sim 61$  Å, diameter ratio  $\sim 1.07$ ) and  $\sim 64$ – $81$  Å (geometric average  $\sim 72$  Å, diameter ratio  $\sim 1.26$ ). A lower density hole with a diameter of  $\sim 17$ – $30$  Å was also shown in each of domains (**Fig. 4E**), in which the  $F_c$  domain hole is the largest. By inserting crystal structures of each domain into its corresponding EM density maps by Chimera<sup>20</sup>, we see a near perfect match to the crystal structure of domains (**Fig. 4F**), suggesting another conformation of the antibody in solution was discovered.

Both above 3D reconstructions are from a single-instance antibody that is free of conformational dynamics and heterogeneity, therefore the IPET-revealed structure can be treated as a “snapshot” of the particular dynamic/fluctuation state in solution at a certain point in time. By aligning two “snapshot” IgG antibody structures based on their  $F_c$  domain, the  $F_{ab}$  domains appear different from each other in location and orientation, the difference between these structures reflects the dynamic fluctuation of the antibody in solution (**Supplementary Video S2**).

**3D reconstruction of an individual peptide-conjugated IgG antibody by IPET.** To uncover the conformational changes of peptide-conjugated antibodies in 3D, we reconstructed two 3D maps from two individual peptide-conjugated antibodies by IPET (**Fig. 4G–L**). Intra-FSC analysis showed that the resolutions were  $\sim 16.5$  Å and  $16.6$  Å respectively (**Supplementary Fig. S1**). The 3D maps at a contour level corresponding to molecular weight (**Fig. 4H and 4K**) show a similar structure to each other in shape and size. For the first particle, the diameters of the three domains are:  $\sim 45$ – $59$  Å (geometric average  $\sim 51$  Å, diameter ratio  $\sim 1.31$ ),  $\sim 48.9$ – $72.7$  Å (geometric average  $\sim 60$  Å, diameter ratio  $\sim 1.49$ ) and  $\sim 42$ – $101$  Å (geometric average  $\sim 65$  Å, diameter ratio  $\sim 2.40$ ) (**Fig. 4H**); For the second particle, the diameter of domains are  $\sim 49$ – $81$  Å (geometric average  $\sim 63$  Å, diameter ratio  $\sim 1.66$ ),  $\sim 49$ – $84$  Å (geometric average  $\sim 64$  Å, diameter ratio  $\sim 1.71$ ) and  $\sim 51$ – $84$  Å (geometric average  $\sim 65$  Å, diameter ratio  $\sim 1.67$ ) (**Fig. 4K**). The domain shape and size show obvious differences from that of an unconjugated antibody. The lower density hole in each domain is not observed, and each domain shows an elongated shape or rod-shape (**Fig. 4H and 4K**). Inserting domain crystal structures (PDB: 1IGT) into its corresponding domain EM density map by Chimera shows a poor match in domain shape, suggesting a conformational change of each domain structure after peptide conjugation (**Fig. 4I and 4L**).

## Discussion

It was generally believed that the domains of antibodies and whole domains were difficult to be imaged by EM because of small molecular size. Our successfully imaged high-resolution detailed structure of small proteins using such a low-end model of TEM (LaB<sub>6</sub> filament) is benefited by the following strategies: i) the sample is prepared by OpNS protocol<sup>14,15</sup>; ii) near-perfect TEM alignment condition (**Supplementary Fig. S2**); iii) near Scherzer focus imaging ( $\sim 0.1$  μm); and iv) higher dose imaging conditions ( $\sim 60$ – $200$  e<sup>-</sup>/Å<sup>2</sup>).

The success of visualizing structural details, such as domains and their holes, is aided by using uranyl formate (UF) as the NS reagent. We previously showed that UF can penetrate the molecular surface

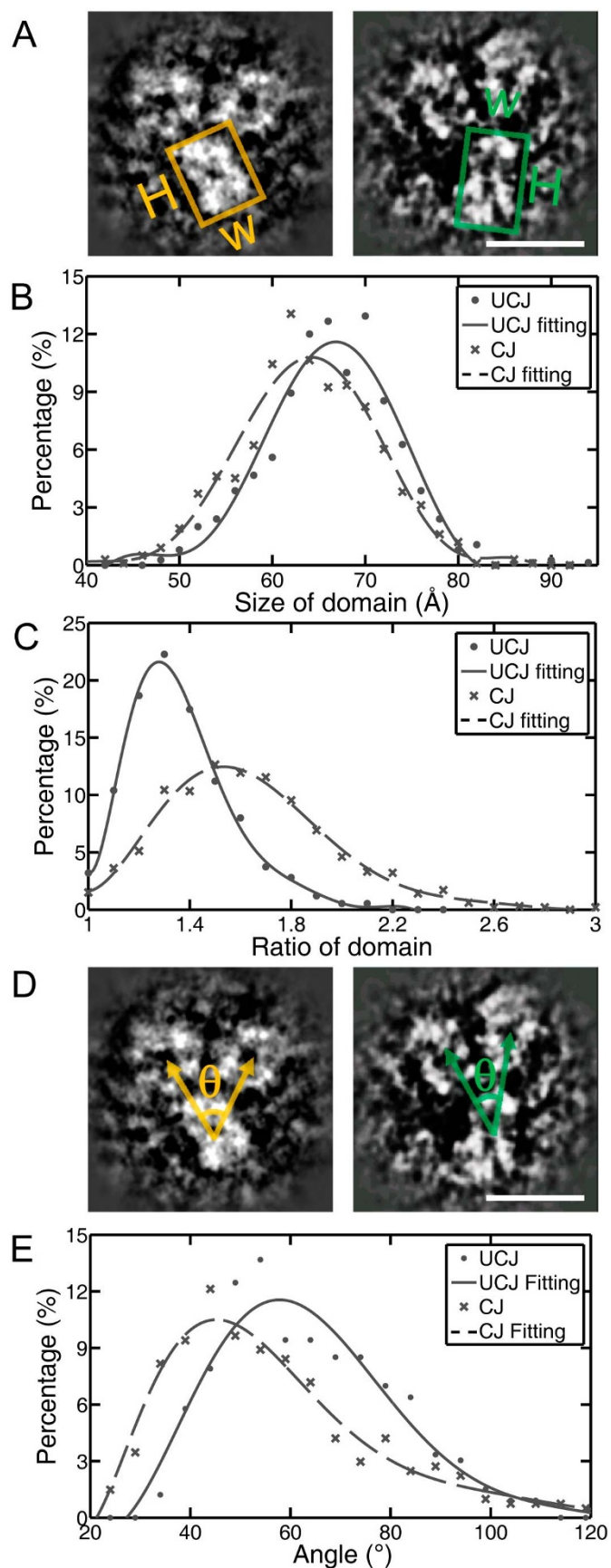


**Figure 3** | Statistical analyses of domain size, shape and fluctuation angles. (A) Two perpendicular diameters on each domain within each particle (left, un conjugated antibody, UCJ; right, conjugated antibody, CJ)

were measured. (B) Histogram of domain diameter geometric mean of antibodies is used for displaying the distribution of the domain size. After normalization and fitting, the peak populations for un conjugated and conjugated occurred at  $66.8 \pm 1.0 \text{ \AA}$  (11.6%) and  $64.2 \pm 1.0 \text{ \AA}$  (10.8%) respectively. (C) Histogram of particle diameter ratios (longest diameter/perpendicular diameter) is used for displaying the distribution of the domain shape. After normalization and fitting, the peak population for the un conjugated antibody occurs at  $1.28 \pm 0.05$  (21.6%), which is similar to that of the conjugated,  $1.53 \pm 0.05$  (12.5%). (D) The antibody fluctuations are represented by the distributions of the angle between  $F_{ab}$  and  $F_c$  domains (left, un conjugated antibody; right, conjugated antibody). (E) Histograms of the fluctuation angles show that the peak populations for un conjugated and conjugated occurred at  $57.8 \pm 2.5^\circ$  (11.6%) and  $45.2 \pm 2.5^\circ$  (10.5%) respectively, after normalization and fitting. Scale bars: 10 nm.

and show high resolution details<sup>14–16</sup>. Those observations challenge the conventional view that NS could only visualize the outer surface of structures. For example, the parallel fringes observed in CETP cryo-PS EM images are well matched to the  $\beta$ -sheet strands within the C-/N-terminal domains of the crystal structure<sup>16</sup>. The mechanism of how UF penetrates the molecular surface is still unknown. One possibility is that the binding of the uranyl cation to available protein carboxyl groups somehow enhances the contrast of the protein main chain.

The success in high-resolution imaging also requires a near-perfect alignment condition and a near Scherzer focus acquisition condition. Two criteria for a near-perfect alignment condition are how many and how far the contrast transfer function (CTF) related Thon rings can be acquired on a continual carbon film image after Fourier transfer. As an example of our good-alignment condition, more than  $\sim 20$  Thon rings ( $\sim 5 \text{ \AA}$ ) can be achieved from a carbon film micrograph that is imaged under a defocus of  $1.6 \text{ \mu m}$  from a LaB<sub>6</sub> filament equipped Zeiss Libra 120 Plus TEM (Supplementary Fig. S2). The high-order of Thon rings achieved from this low-level instrument demonstrated a high-level of coherence that competes well with a field-emission-gun (FEG) equipped Transmission EM that is operating under good alignment condition.

Imaging under a near Scherzer focus is critical for high-resolution imaging of small proteins<sup>17</sup>. The conventional biological strategy for imaging proteins is to use a high-defocus ( $>2 \text{ \mu m}$ ) imaging condition to enhance the overall shape contrast of the protein. The high-defocus can help us to enhance the image contrast by boosting the contribution from low resolution information; consequently we lose a high-percentage of overall structural information. Using a higher defocus, the CTF crosses zero more often (especially for high resolution information), therefore an increased percentage of structural information will be convoluted to zero, those lost information can NOT be recovered by any CTF correcting software. Using the near Scherzer focus condition, the first CTF crosses to zero at the resolution beyond our targeted resolution; therefore no structural information is eliminated by CTF. Although the contrast of small protein images is relatively low from the close-focus conditions, the contrast can be easily raised by simply applying a Gaussian low-pass filter to enhance the overall particle shape.

Antibodies are known to be dynamic and structurally flexible, and co-exist in populations of different structures, rather than in a single rigid conformation determined from X-ray crystallography<sup>21,22</sup>. Antibodies were packed and locked in their lattice positions eliminating their dynamic characters. The fundamental solution to determine the structure of highly dynamic proteins, including antibodies, should be based on a single, individual and unique object/protein.

The first 3D reconstruction of an individual protein reconstructed from NS images was reported in 1974 by the group of Walter Hoppe by ET, in which the 3D reconstruction of a fatty acid synthetase molecule represented a significant achievement, marking the beginning of ET<sup>23</sup>. However, this 3D reconstruction was criticized because

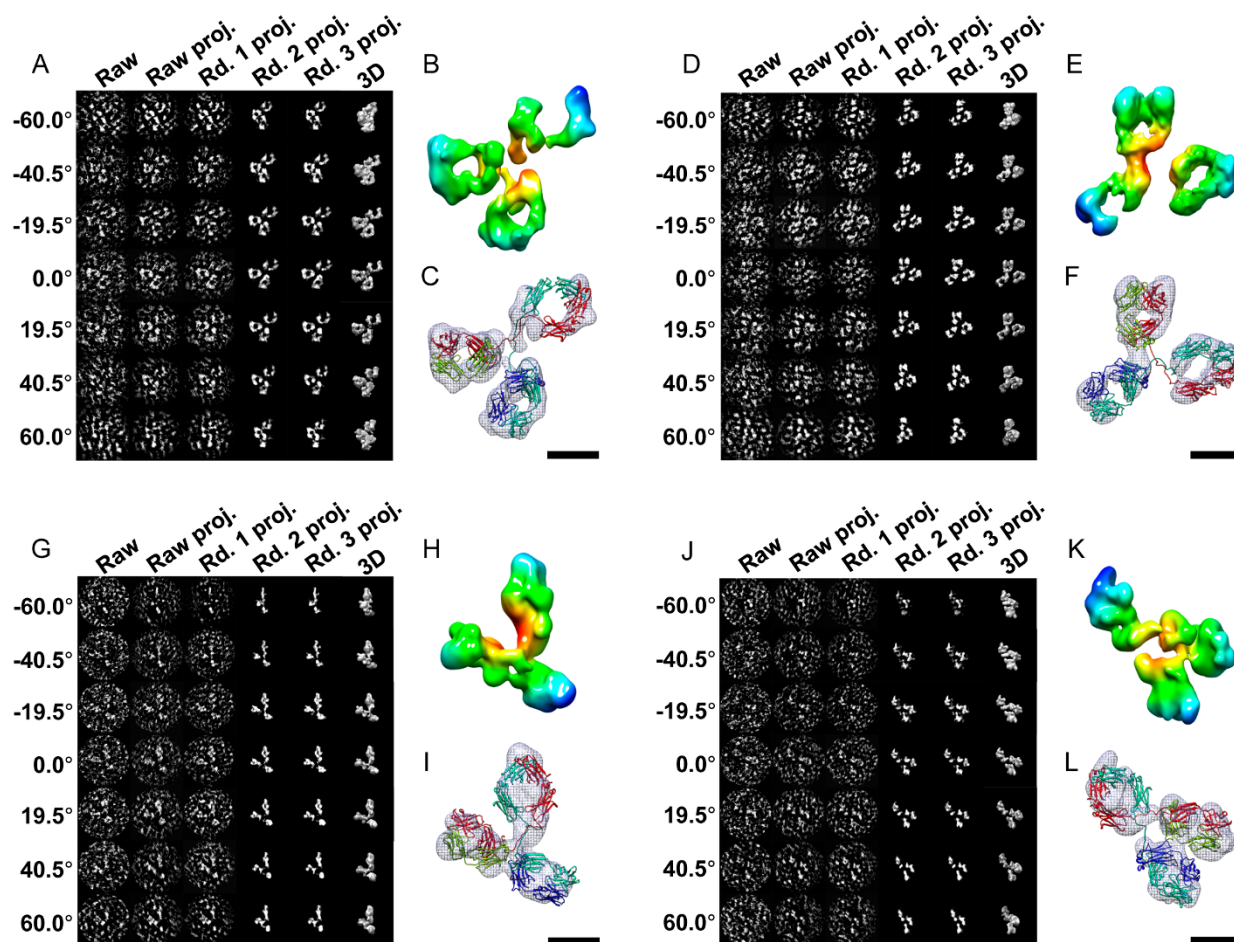


**Figure 4** | 3D reconstructions of individual particles of unconjugated and conjugated IgG antibodies by IPET. (A) An individual unconjugated IgG antibody was imaged by OpNS-ET<sup>17</sup>. Seven tilted views of the same individual unconjugated antibody particle were selected from 81 tilt micrographs and displayed in the leftmost column. By means of the FETR algorithm, the 3D reconstruction was iterated and converged. The corresponding tilting projections of the 3D reconstruction from major iterations are displayed beside the raw images in six columns. (B) The final 3D reconstruction of a targeted individual antibody particle displayed three ring-shaped domains corresponding to the three domains of an IgG antibody<sup>17</sup>. (C) Fitting each domain of the crystal structure (PDB entry 1IGT) into each ring-shaped density of IgG respectively matched well<sup>17</sup>. (D–F) Another individual unconjugated IgG antibody particle was reconstructed by IPET<sup>17</sup>. (G) An individual peptide-conjugated IgG antibody was also imaged and reconstructed. (F) The final 3D reconstruction showed three density rod-shaped blobs corresponding to three domains of this conjugated antibody. (I) Fitting the crystal structure (PDB entry 1IGT) of each domain into these rod-shaped densities of IgG matched poorly. (J–L) Another reconstructed individual peptide-conjugated IgG antibody particle showed similar structural features as the first one. Scale bars: 5 nm.

the molecule receives a radiation dose that exceeds the limit found by Unwin and Henderson by a large factor<sup>23</sup>. 3D reconstruction of an individual antibody was reported by Sandin *et al.*<sup>24</sup>, in which, the 3D map was reconstructed by Constrained Maximum Entropy Tomography (COMET) software from the sample embedded in vitreous ice and imaged under low-dose conditions. The low-resolution 3D reconstruction may provide information to determine the spatial orientation of three domains of a IgG2a antibody, however, detailed image processing procedures were not clearly represented or described. Recently, we reported IPET reconstruction methodology<sup>17</sup> as a new robust strategy/approach which does not require: i) a pre-given initial model, ii) class averaging of multiple molecules or iii) an extended ordered lattice; but still can tolerate small tilt-errors for high-resolution single “snapshot” molecule structural determination. By IPET, two 3D reconstructions ( $\sim 14$  Å) of two IgG antibodies (same as the unconjugated antibodies in this paper) and two 3D reconstructions ( $\sim 36$ – $42$  Å) of two 17 nm high-density lipoproteins (HDL) were respectively reconstructed from OpNS and vitreous ice embedded samples that were imaged under low-dose conditions. As

far as we know, these NS and cryoET reconstructions respectively contain the highest resolution achieved from an individual protein. Our IPET methodology paper provided the detailed step-by-step refinement procedures based on i) a set of simulated cryoET data, ii) two sets of experimental OpNS data (antibodies) and iii) two sets of experimental cryoET data (HDL particles)<sup>17</sup>. Moreover, our IPET paper also provided the detailed strategies (small-area reconstruction to reduce the effects of image distortion along with automatically generated masks and filters), pointed out the common weaknesses in conventional ET reconstruction methods (large-images were used, distortions were ignored), and discussed the cryoET capabilities and limitations (image distortion, dose limitation, resolution limitation, total image number and missing-wedge effect). Considering the general concerns in detailed processing, we provided a video that demonstrates the intermediate processes, including all raw data, 3D projections, volumes and model interpretations (**Supplementary Video S1**). In this research, we implemented this IPET technique to address a real biological question by 3D reconstruction of two peptide-conjugated antibodies. The difference between

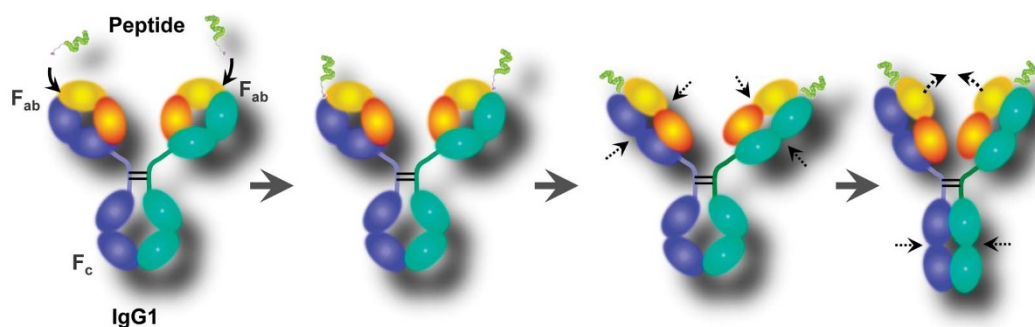


**Figure 5 | A model for peptide-introduced conformational changes of antibody domains.** After peptide conjugation, the  $F_{ab}$  domains may undergo a twist which results in a similar conformational change in the  $F_c$  domain, and such conformational changes may naturally elongate the domains and change the function of the domains by exposing the residues that were inside of the domain surface before conjugation.

conjugated and unconjugated antibodies in 3D reconstructions demonstrates IPET is expanding the new territory of ET in studying protein conformational changes.

Information about antibody dynamics is important to evaluate stability and variety, to identify conformational changes, and to understand antigen recognition for improving rational drug design. Our quantitative analyses of the antibody dynamics and flexibility were performed by statistically analyzing the domain angle distributions. The  $F_{ab}^1-F_c-F_{ab}^2$  angle distribution histogram of unconjugated antibodies shows that the peak population ( $\sim 11.6\%$ ) of the angles is  $\sim 60^\circ$  (Fig. 3E), suggesting the minimal energy conformation is when the centers of three domains are forming a near equilateral triangle shape. The angle of peak population ( $\sim 60^\circ$ ) is similar to that of secretory IgA1 (SIgA1) revealed by X-ray and neutron scattering<sup>25</sup>, but different from the peak angle ( $\sim 180^\circ$ ) revealed from the best-fit models of IgD<sup>26</sup> and IgA1<sup>27</sup> antibodies by X-ray and/or neutron scattering. In contrast, the angle of peak population of the peptide conjugated antibodies is  $\sim 45^\circ$  (Fig. 3E) which is different from any of the above angles.

We found that fusion of the peptide to the  $F_{ab}$  domains causes the conformational change in the  $F_c$  domain, however, the mechanism is unknown. Here, we proposed two mechanism models to understand the peptide-induced conformational changes. First model is “steric model”, in which, the two  $F_{ab}$  and  $F_c$  domains may reorient themselves in order to accommodate both  $\alpha$ -helices of peptides due to steric effects. Second model is “trigger model” (Fig. 5 and Supplementary Fig. S3), in which, two sets of pairs of  $\beta$ -strands of two  $F_{ab}$  domains were twisted together after peptide conjugation that may serve as a trigger and lead to a conformational change in the  $F_c$  domain (Supplementary Video S2). The second model is similar to the antigen-induced mechanism model, in which the attachment of the  $F_{ab}$  fragment to the antigen triggered the  $F_c$  domain activity that participates in complement fixation and the initiation of other effector activities. There are three mechanisms of antigen-induced conformational change: i) the “distortive mechanism”, with the assumed tension generated by antigen binding forcing structural alterations ultimately involving the  $F_c$  fragment; ii) the “allosteric mechanism”, with the postulated operation of a structural “all or none” switching mechanism in antibodies that triggers effector activation<sup>28</sup>; iii) the “associative mechanism”, with a pre-condition in that the accumulation of antibodies in immune complexes is necessary to induce effector activities. Legitimacy of the antigen-induced models is debated. Supporting experiments include that: i) the circular polarization of fluorescence suggests that the disulfide bonds at the hinge region of the antibody are required to translate the conformational change from the  $F_{ab}$  to the  $F_c$  domain<sup>29</sup>; ii) X-ray crystallography reports a  $15^\circ$  conformation change of the  $F_{ab}$  domains of OPG2 antibody by an antigen,  $\beta 3$  peptide, through carbonyl fragments of  $F_{ab}$  domains<sup>30</sup>. Unfortunately, the small and

diverse changes generated by the binding of antigens in most observed cases by crystallography cannot be generalized or identified with signaling<sup>31–35</sup>.

Validation of above peptide-induced models can be conducted by: i) using shorter  $\alpha$ -helix contained peptides to bind these antibodies which may reduce overall steric effects, therefore reducing the conformational changes of these antibodies; ii) direct visualization of the peptide location and orientation on the surface of these antibodies. Our OpNS-EM method used in this research has not yet demonstrated a sufficient resolution capability for directly imaging the  $\alpha$ -helix of the peptide in these peptide-conjugated antibodies. However, one promising method for future high-resolution imaging of these peptides is using our newly reported cryo-PS-EM method that has demonstrated a high-resolution capability for direct visualization of the likely secondary-structural detail from a small protein, 53kDa cholesteryl ester transfer protein (CETP)<sup>16</sup>.

In summary, the peptide conjugation to the  $F_{ab}$  domains produced conformational changes in the  $F_c$  domain; ultimately changing antibody function. The success in imaging and reconstructing this highly dynamic and heterogeneous antibody suggests the OpNS and IPET can be used as novel and efficient tools to impact drug design.

## Methods

**Synthesis and isolation of conjugated antibodies.** Unconjugated samples (20.0 mg/ml), monoclonal antibody IgG subclass 1 (h38C2, humanized version of m38C2), are expressed in HEK-293 cells, purified using protein A/G chromatography<sup>8</sup>. Conjugated antibody samples are h38C2 conjugated with modified exendin peptide (H(Aib)TFTSDLSKQMEEEAVRLFIEWLKNKGGPSSGAPPPSK, 65% helix in molecular weight of 4959.52)<sup>36</sup>. The specific linker is comprised of a peptide and is designed to be recognized and covalently bound only by the active binding site of the antibody. The conjugation to a reactive lysine is on the complementarity determining region (CDR) loop of the antibody. The conjugated antibody named CovX-body by Pfizer CovX LLC is a new class of chemical entities that possesses the biologic actions of the peptide and the extended half-life of the antibody. The utility of this technology has been successfully demonstrated by enhancing the pharmacokinetic and pharmacodynamics profiles of peptides and small molecules across several disease areas.

The peptide was synthesized and covalently linked to the reactive lysine of the unconjugated antibody<sup>36</sup>. Size exclusion chromatography/mass spectrometry (SEC/MS) is used for the characterization of conjugated antibody by analysis of the intact antibody. The intact mass is useful for determination of the number of peptide drug molecules added to the antibody since the mass of the product increases in proportion to the mass and number of peptide drugs added.

Electrospray ionization MS is used to acquire the mass spectrum and the resulting data is a mixture of charged states. The multi-charged mass spectrum is acquired from the SEC/MS chromatogram by averaging the spectra over a one minute elution time, then the spectrum (mass/charge versus intensity) is deconvoluted into the zero charge state spectrum (mass versus intensity). The material tested consisted of a mixture of antibodies with 72.3% 2 peptides per antibody and 7.5% with no conjugates added (Supplementary Fig. S4). The remainder was a mixture of 1 (16.9%) or 3 (3.2%) conjugates added per antibody.

**EM specimen preparation by the optimized NS (OpNS) protocol.** Both unconjugated and conjugated antibody (molecular mass  $\sim 150$  kDa) samples were prepared with the optimized NS protocol<sup>14,15</sup>. The conjugated antibody and



unconjugated antibody complexes were diluted to 0.05 mg/ml with Dulbecco's phosphate-buffered saline (DPBS: 2.7 mM KCl, 1.46 mM  $\text{KH}_2\text{PO}_4$ , 136.9 mM NaCl, and 8.1 mM  $\text{Na}_2\text{HPO}_4$ ; Invitrogen) buffer. An aliquot (~3  $\mu\text{l}$ ) was placed on a thin-carbon-coated 300 mesh copper grid (Cu-300CN, Pacific Grid-Tech, San Francisco, CA) that had been glow-discharged. After ~1 min, excess solution was blotted with filter paper, and then followed with a procedure of washing and staining as described<sup>14,15</sup>, in which three drops of 1% (w/v) uranyl formate (UF) negative stain on parafilm were then applied successively before being nitrogen-air-dried at room temperature. Since UF solutions are light-sensitive and unstable, the operation was mostly performed in the dark<sup>14,15</sup>.

**Electron microscopy data acquisition and image pre-processing.** The OpNs micrographs were acquired at room temperature on a Gatan UltraScan 4 K × 4 K CCD by a Zeiss Libra 120 Plus transmission electron microscope (Carl Zeiss NTS) with 20-eV in-column energy filter operating at 120 kV at 80,000x magnification under Scherzer focus, and a FEI Tecnai 20 transmission electron microscope (Philips Electron Optics-FEI) operating at 200 kV at 80,000x or 150,000x magnification under Scherzer focus. Each pixel of the micrographs corresponded to 1.48 Å, 1.41 Å or 0.75 Å in the specimens. A total ~58 micrographs were acquired and a total of more than ~250 particles from unconjugated antibody samples and a total of more than ~332 particles from conjugated antibody samples were windowed and selected for statistical analyses.

Micrographs were processed with EMAN and FREALIGN software packages<sup>12,37</sup>. The defocus and astigmatism of each micrograph were examined by fitting the contrast transfer function (CTF) parameters with its power spectrum by *ctffind3* in the FREALIGN software package<sup>37</sup>. Micrographs with relatively larger defocus (>0.2  $\mu\text{m}$ ) or distinguishable drift effects were excluded. Only isolated particles from the NS-EM images were initially selected and windowed using the *boxer* program in the EMAN<sup>12</sup> and then manually adjusted.

**Electron tomography data collection and image pre-processing.** Electron tomography data of unconjugated and conjugated antibody specimens were acquired under a less than 2  $\mu\text{m}$  defocus with a high-sensitivity 4,096 × 4,096 pixel Gatan UltraScan CCD camera at 80,000 × magnifications, and with the same Zeiss Libra 120 TEM and FEI T20 TEM (each pixel of the micrograph corresponds to 1.48 Å and 1.41 Å in the specimens respectively). The specimens mounted on a Gatan 626 high-tilt room-temperature holder were tilted at angles ranging from -60° to 60° in steps of 1.5° for unconjugated antibodies and -70.5° to 70.5° in steps of 1.5° for conjugated antibodies. The total illumination electron dose was ~200  $\text{e}^-/\text{Å}^2$  or slightly higher. The tilt series of tomographic data were controlled and imaged by manual operation and by Gatan tomography software (Zeiss Libra 120 TEM) and UCSF Tomography software (FEI T20 TEM) that were preinstalled in the microscopes<sup>38</sup>.

Micrographs were initially aligned together with the IMOD software package<sup>39</sup> and UCSF Tomography<sup>38</sup>. The defocus near the tilt-axis area of each tilt micrograph was examined by fitting the contrast transfer function (CTF) parameters with its power spectrum by *ctffind3* in the FREALIGN software package<sup>37</sup> and then examined by *ctfit* (EMAN software package)<sup>12</sup>. The CTF was then corrected by TOMOCTF<sup>40</sup>. The tilt series of each antibody particle image in windows of 200 × 200 pixels (~296 × 296 Å or 282 × 282 Å) were semi-automatically tracked and selected by IPET software.

**Statistical analyses of the domain size, shape and angles.** For statistical analysis of domain size and shape, a total of 58 micrographs were used. Each micrograph was Gaussian low-pass filtered before particles were identified and selected by examining the particles at 4x zoom. Particles were picked automatically and manually checked to remove overlapping or damaged particles with *boxer*<sup>12</sup>. More than 250 particle images from the micrographs of each condition were used for statistical analysis of particle size distribution. Domain size was determined by measuring diameters in two orthogonal directions, one of which was the longest dimension of the particle. The geometric mean (the square root of the product) of the perpendicular diameters was used to represent the domain size/diameter. The aspect ratio between the longest diameter and its perpendicular diameter was calculated to represent the domain shape. Histograms for the size of each domain image were generated with a sampling step of 2.0 Å. Each histogram was fitted with a ninth degree polynomial function in Matlab for data analysis. Histograms of domain ratios were computed and fitted in the same manner as domain size, but with a sampling step of 0.10.

For measuring the angle between  $F_{ab}$  domains and the  $F_c$  domain, two  $F_{ab}$  domains were distinguished based on the following criteria: i) two  $F_{ab}$  domains were most similar to each other in size, but smaller than the  $F_c$  domain; ii) the distance between the center of each  $F_{ab}$  domain to the  $F_c$  domain are closer to each other; iii) the distance between two  $F_{ab}$  domain centers were not longer than 120 Å; iv) two major pieces of  $F_{ab}$  domain densities were distributed perpendicularly against the radius direction viewed from the center of the particle; while two major pieces of the  $F_c$  domain were distributed along the radial direction. The center coordinates of each domain were measured by using *boxer*<sup>12</sup>. The centers of the domain were used to compute the angles between the  $F_{ab}$  domains of each antibody particle by a Python batch program. Histograms for the angle were generated with a sampling step of 5.0°. Each histogram was fitted with a ninth degree polynomial function in Matlab for data analysis.

**Individual-particle electron tomography (IPET) 3D reconstruction.** The IPET method<sup>17</sup> contains two phases: the electron tomography (ET) data collection with image preprocessing, and a focused electron tomography reconstruction (FETR)

algorithm. In the first phase, the single-instance of a particle was imaged by ET. The contrast transfer function (CTF) of the whole-micrograph-size tilt images were determined, and then corrected after the tilt images were pre-center aligned. The small image containing only a targeted particle was selected and windowed from each tilted whole-micrograph. Directly back-projected these small-images into a 3D map to be used as an initial model, the 3D reconstruction refinements were performed via three rounds of refinement loops by FETR algorithm. Each round was essentially the same, except that different automatic-generated masks were applied. In the first round, circular Gaussian-edge masks were used; in the second round, particle-shaped masks were used. In the third round, the last particle-shaped mask of the second round was used in association with an additional interpolation method during the determination of the translational parameters. Each round of refinement loops contains the same iteration algorithm, FETR. Within each iteration, the 3D map from the previous iteration (or initial model for the first iteration) was used as the "initial" model for this current round. The projections of the "initial" model were used as the references for images alignment. Before translational parameter searching, a dynamic Gaussian low-pass filter and automatically generated mask were applied to both the references and tilt images. In the last round, the translation searching was carried out to sub-pixel accuracy by interpolating the particle images by 10 times in each dimension using the triangular interpolation technique.

The three domains of the crystal structure (PDB entry 1IGT<sup>18</sup>) were fitted into the final IPET 3D density map by using a rigid-body fitting option in UCSF Chimera<sup>20</sup>. The bridging loops between the  $F_{ab}$  and  $F_c$  domains were then manually connected.

**Intra-Fourier shell correlation (intra-FSC) analysis.** To analyze tomographic 3D reconstructions, the center-refined raw ET images were split into two groups based on having an odd- or even-numbered index in the order of tilt angles<sup>17</sup>. Each group was used to generate a 3D reconstruction; these two 3D reconstructions were then used to compute the FSC curve over their corresponding spatial frequency shells in Fourier space (using the "RF 3" command in SPIDER)<sup>13</sup>. Since this FSC computation used a single set of raw ET images, we call it intra-FSC to distinguish it from the regular FSC that is computed between two independent 3D reconstructions<sup>17</sup>. The frequency at which the intra-FSC curve falls to a value of 0.5 (called intra- $f_{0.5}$ ) was used to represent the resolution of the final IPET 3D density map.

- Otvos, L. Jr., Peptide-based drug design: here and now. *Methods in molecular biology* **494**, 1–8 (2008).
- Friden, P. M. et al. Anti-transferrin receptor antibody and antibody-drug conjugates cross the blood-brain barrier. *Proceedings of the National Academy of Sciences of the United States of America* **88**, 4771–4775 (1991).
- Allen, T. M. Long-circulating (sterically stabilized) liposomes for targeted drug delivery. *Trends in pharmacological sciences* **15**, 215–220 (1994).
- Sellers, W. R. & Fisher, D. E. Apoptosis and cancer drug targeting. *The Journal of clinical investigation* **104**, 1655–1661 (1999).
- Hollopeter, G. et al. Identification of the platelet ADP receptor targeted by antithrombotic drugs. *Nature* **409**, 202–207 (2001).
- Carven, G. J. et al. Monoclonal antibodies specific for the empty conformation of HLA-DR1 reveal aspects of the conformational change associated with peptide binding. *The Journal of biological chemistry* **279**, 16561–16570 (2004).
- Li, L. et al. Antitumor efficacy of a thrombospondin 1 mimetic CovX-body. *Translational oncology* **4**, 249–257 (2011).
- Doppalapudi, V. R. et al. Chemically programmed antibodies: endothelin receptor targeting CovX-Bodies. *Bioorganic & medicinal chemistry letters* **17**, 501–506 (2007).
- James, L. C., Roversi, P. & Tawfik, D. S. Antibody multispecificity mediated by conformational diversity. *Science* **299**, 1362–1367 (2003).
- James, L. C. & Tawfik, D. S. Conformational diversity and protein evolution—a 60-year-old hypothesis revisited. *Trends in biochemical sciences* **28**, 361–368 (2003).
- Ren, G. et al. Model of human low-density lipoprotein and bound receptor based on cryoEM. *Proceedings of the National Academy of Sciences of the United States of America* **107**, 1059–1064 (2010).
- Ludtke, S. J., Baldwin, P. R. & Chiu, W. EMAN: semiautomated software for high-resolution single-particle reconstructions. *Journal of structural biology* **128**, 82–97 (1999).
- Frank, J. et al. SPIDER and WEB: processing and visualization of images in 3D electron microscopy and related fields. *Journal of structural biology* **116**, 190–199 (1996).
- Zhang, L. et al. An optimized negative-staining protocol of electron microscopy for apoE4 POPC lipoprotein. *Journal of lipid research* **51**, 1228–1236 (2010).
- Zhang, L. et al. Morphology and structure of lipoproteins revealed by an optimized negative-staining protocol of electron microscopy. *Journal of lipid research* **52**, 175–184 (2011).
- Zhang, L. et al. Structural basis of transfer between lipoproteins by cholesteryl ester transfer protein. *Nat Chem Biol* **8**, 342–349 (2012).
- Zhang, L. & Ren, G. IPET and FETR: experimental approach for studying molecular structure dynamics by cryo-electron tomography of a single-molecule structure. *PLoS one* **7**, e30249 (2012).
- Harris, L. J., Larson, S. B., Hasel, K. W. & McPherson, A. Refined structure of an intact IgG2a monoclonal antibody. *Biochemistry* **36**, 1581–1597 (1997).
- James, L. C. & Tawfik, D. S. The specificity of cross-reactivity: promiscuous antibody binding involves specific hydrogen bonds rather than nonspecific





- hydrophobic stickiness. *Protein science : a publication of the Protein Society* **12**, 2183–2193 (2003).
20. Pettersen, E. F. *et al.* UCSF Chimera--a visualization system for exploratory research and analysis. *Journal of computational chemistry* **25**, 1605–1612 (2004).
  21. Harris, L. J., Skaletsky, E. & McPherson, A. Crystallographic structure of an intact IgG1 monoclonal antibody. *Journal of molecular biology* **275**, 861–872 (1998).
  22. Harris, L. J. *et al.* The three-dimensional structure of an intact monoclonal antibody for canine lymphoma. *Nature* **360**, 369–372 (1992).
  23. Frank, J. In *Electron Tomography: Methods for Three-Dimensional Visualization of Structures in the Cell*, Edn. 2. (ed. J. Frank) 6 (Pringer, 2006).
  24. Sandin, S., Ofverstedt, L. G., Wikstrom, A. C., Wrangle, O. & Skoglund, U. Structure and flexibility of individual immunoglobulin G molecules in solution. *Structure* **12**, 409–415 (2004).
  25. Bonner, A., Almogren, A., Furtado, P. B., Kerr, M. A. & Perkins, S. J. Location of secretory component on the Fc edge of dimeric IgA1 reveals insight into the role of secretory IgA1 in mucosal immunity. *Mucosal immunology* **2**, 74–84 (2009).
  26. Sun, Z. *et al.* Semi-extended solution structure of human myeloma immunoglobulin D determined by constrained X-ray scattering. *Journal of molecular biology* **353**, 155–173 (2005).
  27. Furtado, P. B. *et al.* Solution structure determination of monomeric human IgA2 by X-ray and neutron scattering, analytical ultracentrifugation and constrained modelling: a comparison with monomeric human IgA1. *Journal of molecular biology* **338**, 921–941 (2004).
  28. Oda, M., Kozono, H., Morii, H. & Azuma, T. Evidence of allosteric conformational changes in the antibody constant region upon antigen binding. *International immunology* **15**, 417–426 (2003).
  29. Schlessinger, J., Steinberg, I. Z., Givol, D., Hochman, J. & Pecht, I. Antigen-induced conformational changes in antibodies and their Fab fragments studied by circular polarization of fluorescence. *Proceedings of the National Academy of Sciences of the United States of America* **72**, 2775–2779 (1975).
  30. Kodandapani, R. *et al.* Conformational change in an anti-integrin antibody: structure of OPG2 Fab bound to a beta 3 peptide. *Biochemical and biophysical research communications* **251**, 61–66 (1998).
  31. Guddat, L. W., Shan, L., Anchin, J. M., Linthicum, D. S. & Edmundson, A. B. Local and transmitted conformational changes on complexation of an anti-sweetener Fab. *Journal of molecular biology* **236**, 247–274 (1994).
  32. Colman, P. M. *et al.* Three-dimensional structure of a complex of antibody with influenza virus neuraminidase. *Nature* **326**, 358–363 (1987).
  33. Wilson, I. A. & Stanfield, R. L. Antibody-antigen interactions: new structures and new conformational changes. *Current opinion in structural biology* **4**, 857–867 (1994).
  34. Schulze-Gahmen, U., Rini, J. M. & Wilson, I. A. Detailed analysis of the free and bound conformations of an antibody. X-ray structures of Fab 17/9 and three different Fab-peptide complexes. *Journal of molecular biology* **234**, 1098–1118 (1993).
  35. Bhat, T. N., Bentley, G. A., Fischmann, T. O., Boulot, G. & Poljak, R. J. Small rearrangements in structures of Fv and Fab fragments of antibody D1.3 on antigen binding. *Nature* **347**, 483–485 (1990).
  36. Murphy, R. E. *et al.* Combined use of immunoassay and two-dimensional liquid chromatography mass spectrometry for the detection and identification of metabolites from biotherapeutic pharmacokinetic samples. *Journal of pharmaceutical and biomedical analysis* **53**, 221–227 (2010).
  37. Grigorieff, N. FREALIGN: high-resolution refinement of single particle structures. *Journal of structural biology* **157**, 117–125 (2007).
  38. Zheng, S. Q. *et al.* UCSF tomography: an integrated software suite for real-time electron microscopic tomographic data collection, alignment, and reconstruction. *Journal of structural biology* **157**, 138–147 (2007).
  39. Kremer, J. R., Mastronarde, D. N. & McIntosh, J. R. Computer visualization of three-dimensional image data using IMOD. *Journal of structural biology* **116**, 71–76 (1996).
  40. Fernandez, J. J., Li, S. & Crowther, R. A. CTF determination and correction in electron cryotomography. *Ultramicroscopy* **106**, 587–596 (2006).

## Acknowledgements

We thank Dr. Shengli Zhang, and Mrs. James Song for their discussion and editing comments. This work was supported by the Office of Science, Office of Basic Energy Sciences of the United States Department of Energy (contract no. DE-AC02-05CH11231) and partially supported by the William Myron Keck Foundation (no: 011808), QB3-Pfizer research grant (no: P0030609 and P0024086), and National Heart, Lung, and Blood Institute of the National Institutes of Health (no. R01HL115153).

## Author contributions

G.R., A.K. and G.W. initiated and designed the project; A.K. and G.W. provided the samples; G.R. and L.Z. collected the data; H.T., L.Z. and G.R. measured the sizes and shapes. H.T., L.Z. and G.R. solved the 3D structure; G.R., H.T., M.R. and L.Z. analyzed and interpreted the data; H.T., L.Z. and G.R. drafted the initial manuscript; H.T., L.Z., A.K., L.H., G.W., M.R. and G.R. discussed and revised the manuscript.

## Additional information

**Data deposition:** The IPET EM density maps of peptide-conjugated antibody #1 and #2 are available from the EMDB as EMDB ID 2285 and 2286 respectively. The EMDB IDs of IEPT EM density maps of IgG1 antibody #1 and #2 are 2021 and 2022.

**Supplementary information** accompanies this paper at <http://www.nature.com/scientificreports>

**Competing financial interests:** AK and GW are employees of Pfizer Inc., and research was partially supported by Pfizer Inc. Pfizer Inc. develops and markets medicines to treat cancer disease.

**License:** This work is licensed under a Creative Commons Attribution-NonCommercial-NoDerivs 3.0 Unported License. To view a copy of this license, visit <http://creativecommons.org/licenses/by-nc-nd/3.0/>

**How to cite this article:** Tong, H. *et al.* Peptide-Conjugation Induced Conformational Changes in Human IgG1 Observed by Optimized Negative-Staining and Individual-Particle Electron Tomography. *Sci. Rep.* **3**, 1089; DOI:10.1038/srep01089 (2013).